CrossMark

ARTICLE

Template-Free Synthesis of Sb_2S_3 Hollow Microspheres as Anode Materials for Lithium-Ion and Sodium-Ion Batteries
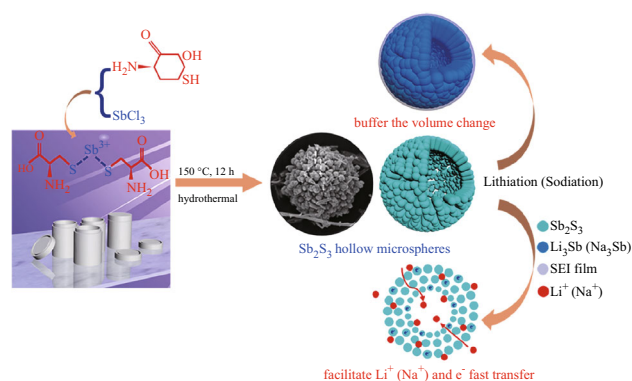
Jianjun Xie[1] · Li Liu[1,2] · Jing Xia[1] · Yue Zhang[1] · Min Li[1] · Yan Ouyang[1] · Su Nie[1] · Xianyou Wang[1]

Highlights

- Sb_2S_3 hollow microspheres have been successfully synthesized by a simple hydrothermal reaction using $SbCl_3$ and L-cysteine as raw materials without adding any surfactants.
- The novel architecture combines the merits of nanometer size, hollow interior, and 3D hierarchical structure.
- The material presents remarkable cycling performance and outstanding rate capability in lithium-ion batteries and also exhibits superior sodium-storage capabilities in sodium-ion batteries.

Abstract Hierarchical Sb_2S_3 hollow microspheres assembled by nanowires have been successfully synthesized by a simple and practical hydrothermal reaction. The possible formation process of this architecture was investigated by X-ray diffraction, focused-ion beam-scanning electron microscopy dual-beam system, and transmission electron microscopy. When used as the anode material for lithium-ion batteries, Sb_2S_3 hollow microspheres manifest excellent rate property and enhanced lithium-storage capability and can deliver a discharge capacity of 674 mAh g^{-1} at a current density of 200 mA g^{-1} after 50 cycles. Even at a high current density of 5000 mA g^{-1}, a discharge capacity of 541 mAh g^{-1} is achieved. Sb_2S_3 hollow microspheres also display a prominent sodium-storage capacity and maintain a reversible discharge capacity of 384 mAh g^{-1} at a current density of 200 mA g^{-1} after 50 cycles. The remarkable lithium/sodium-storage property may be attributed to the synergetic effect of its nanometer size and three-dimensional hierarchical architecture, and the outstanding stability property is attributed to the sufficient interior void space, which can buffer the volume expansion.

✉ Li Liu
liulili1203@126.com

1 National Base for International Science and Technology Cooperation, National Local Joint Engineering Laboratory for Key Materials of New Energy Storage Battery, Hunan Province Key Laboratory of Electrochemical Energy Storage and Conversion, School of Chemistry, Xiangtan University, Xiangtan 411105, People's Republic of China

2 Key Laboratory of Advanced Energy Materials Chemistry (Ministry of Education), Nankai University, Tianjin 300071, People's Republic of China

1 Introduction

Owing to the numerous inherent advantages of lithium-ion batteries (LIBs), they have been generally applied in many fields and display good prospect in large-scale energy-storage systems [1–5]. However, sodium-ion batteries (NIBs) have attracted much attention as a potential substitute to LIBs [6–8]. In recent years, there have been successful studies into the development of cathode materials for LIBs and NIBs [9, 10]. Therefore, many researchers have focused on exploring potential suitable anode materials for future LIBs and NIBs [11–15]. Among the many suitable anode materials for LIBs and NIBs, antimony sulfide (Sb_2S_3) is a highly anisotropic semiconductor that crystallizes with a layered structure, and it has received significant attention owing to its high theoretical specific capacity (947 mAh g^{-1}) and superior lithium/sodium-storage performance [14–16]. For instance, Zhou et al. [17] demonstrated Sb_2S_3 nanorod bundles with a fine cyclability of 614 mAh g^{-1} at a current density of 100 mA g^{-1} after 30 cycles, as well as an excellent rate capability of 400 mAh g^{-1} at a current density of 500 mA g^{-1} in LIBs. Yi et al. [18] reported Sb_2S_3 with a discharge capacity of 548 mAh g^{-1} at a current density of 100 mA g^{-1} after 100 cycles in LIBs. Discharge capacities of 659.7, 564.9, 434.2, and 300.5 mAh g^{-1} are achieved at current densities of 100, 200, 500, and 1000 mA g^{-1}, respectively. Denis et al. [19] exhibited the cyclic property of commercial Sb_2S_3 at a current density of 50 mA g^{-1} in NIBs. During the initial 10 cycles, the discharge capacity of commercial Sb_2S_3 increases from 337 to 419 mAh g^{-1}. However, after 50 cycles, it decreases to less than 200 mAh g^{-1}, which is under 50% of the maximum capacity. Pan et al. [20] reported the template-free synthesis of Sb_2S_3 microtubes, whose respective initial discharge and charge capacities are 910 and 400 mAh g^{-1} at a current density of 100 mA g^{-1} in NIBs, respectively. After 20 cycles, the capacity remains at 201 mAh g^{-1}.

Over the past few decades, many studies have been devoted to the exploration of Sb_2S_3 with various particle sizes, morphologies, coating, as well as composites for enhancing rate capability and cycling stability. Recently, the design and synthesis of three-dimensional (3D) hierarchical architecture Sb_2S_3 materials have attracted considerable attention, owing to their capability to effectively improve electrochemical performance by enlarging the contact surface area between the electrolyte and electrode, reducing the transport pathway of electrons and Li^+/Na^+, as well as accommodating the volume expansion [21–25].

Here, Sb_2S_3 hollow microspheres have been effectively synthesized by a straightforward hydrothermal reaction employing L-cysteine and $SbCl_3$ as raw materials without adding any surfactants. This novel architecture combines the merits of hollow and 3D hierarchical structures. As expected, the Sb_2S_3 hollow microspheres exhibit superior lithium/sodium-storage capacity and outstanding rate property.

2 Experimental Section

2.1 Material Synthesis

The Sb_2S_3 samples were prepared using a hydrothermal reaction. To obtain Sb_2S_3 hollow microspheres, 3 mmol L-cysteine was dissolved in 30 mL distilled water under magnetic stirring for 15 min to obtain a colorless solution. Then, 30 mL distilled water and 2 mmol $SbCl_3$ were systematically poured into the beaker under stirring for 35 min to produce a milky suspension liquid. Afterward, the above solution was transferred into an 80-mL Teflon-lined stainless-steel autoclave and then maintained at 150 °C for 12 h. The Sb_2S_3 was gathered and washed several times with absolute ethyl alcohol and deionized water, and dried at 80 °C for 5 h in vacuum. Comparable samples were prepared using a similar procedure at alter hydrothermal reaction temperatures of 120 °C and 180 °C, respectively. These three samples are denoted as Sb_2S_3-120, Sb_2S_3-150, and Sb_2S_3-180 according to the variation of reaction temperature.

2.2 Electrochemical Measurements

The work electrode was prepared by mixing the carboxymethyl cellulose Na salt (CMC), acetylene black, and active material in the mass ratio of 1:1:3, after which the viscosity was varied with distilled water and magnetic stirring overnight. The loading mass of the active material is around 1 mg cm^{-2}. For LIBs, the testing batteries were assembled with the working electrode already prepared, and with Celgard 2300 film as the separator, lithium metal as the reference/counter electrode, and 1 M $LiPF_6$ in dimethyl carbonate (DMC)/ethylene carbonate (EC) (1:1 v/v) as the electrolyte. However, NIBs were assembled with glass fiber film (Whatman GF/D) as the separator, metal sodium as the reference/counter electrode, and 1 M $NaClO_4$ in ethylene carbonate (EC)/propylene carbonate (PC) (1:1 v/v) as the electrolyte. All batteries were fabricated in an argon-filled glove box with H_2O and O_2 values below 1 ppm. The charge/discharge measurements of the Sb_2S_3 electrodes were taken on a Neware battery test system at room temperature.

2.3 Material Characterization

The morphology, structure, and interplanar distance of the samples were verified using a focused-ion beam-scanning electron microscope dual-beam system (FIB-SEM, FEI Helios Nanolab 600i), transmission electron microscopy (TEM), and high-resolution transmission electron microscopy (HRTEM JEOL JEM-2100F). X-ray diffraction (XRD) data were obtained using a Rigaku D/MAX-2500 power diffractometer for $2\theta = 10°–70°$. Cyclic voltammograms (CV) and electrochemical impedance spectroscopy (EIS) tests were executed on a Zahner Zennium electrochemical workstation.

3 Results and Discussion

3.1 Characterization of the As-Prepared Sb_2S_3

The phase composition and crystal structure of the as-prepared Sb_2S_3 samples were identified by XRD, as illustrated in Fig. 1. The diffraction peaks of Sb_2S_3-120 can be indexed as orthorhombic Sb_2S_3 phase (space group: Pbnm) and monoclinic $Sb_8O_{11}Cl_2$ phase (space group: C2m), which are in accordance with the standard date files PDF 42-1393 and PDF 77-1583, respectively. However, all diffraction peaks of Sb_2S_3-150 and Sb_2S_3-180 agree well with the standard diffraction patterns of orthorhombic Sb_2S_3 (PDF 42-1393, space group: Pbnm), and no other impure phases were detected. Furthermore, the sharp and narrow peaks indicate that these two samples are highly crystalline.

The morphologies and sizes of these three samples were characterized by FIB-SEM and TEM, as shown in Fig. 2.
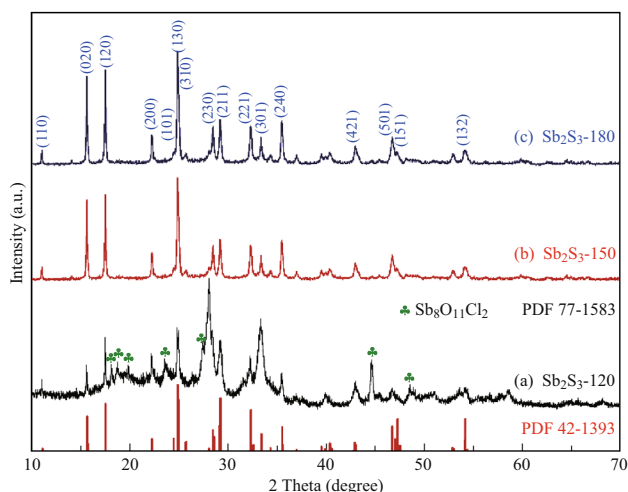

Fig. 1 XRD patterns of as-prepared **a** Sb_2S_3-120, **b** Sb_2S_3-150, and **c** Sb_2S_3-180 samples

The feature images of the prepared Sb_2S_3-120 sample are exhibited in Fig. 2a, d, g, and have numerous nanowires with diameters ranging from 80 to 100 nm. Moreover, densely aggregated primary nanowires can be clearly observed. When the reaction temperature was increased to 150 °C (Sb_2S_3-150), multiple 2–3 μm microsphere structures were obtained (Fig. 2b, e, h). More interestingly, by dissecting a randomly selected particle of the Sb_2S_3-150 sample, the FIB-SEM images reveal their hollow interior, and the 3D hollow microsphere structures are in fact built from irregularly shaped nanowires (Fig. S1). It has been reported that this 3D hierarchical hollow architecture will facilitate electrolyte percolation and increase the contact surface area between the electrolyte and electrode [26–30]. Besides, owing to the multiple levels of the structure, this structure can provide both large surface and firm stability [22, 30]. With a further increase in the reaction temperature to 180 °C, Sb_2S_3-180 shows rough solid spheres (Fig. 2c, f, i). It is evident that the reaction temperature has a significant effect on the morphology of the materials.

To evaluate the structure and element distribution of the Sb_2S_3-150 sample, TEM image of a randomly selected particle of Sb_2S_3-150 was acquired and is shown in Fig. 3a. It is clearly seen that the Sb_2S_3-150 microsphere has a hollow interior structure. The HRTEM image of the Sb_2S_3-150 sample shown in Fig. 3b. Figure 3b exhibits clear lattice fringes and showed that the interplanar distance between the adjacent lattices is 0.37 and 0.56 nm, corresponding to the (101) and the (200) planes of orthorhombic Sb_2S_3 (space group: Pbnm), respectively. The fast Fourier transform (FFT) pattern (Fig. 3c) reveals that the observed reflections of the Sb_2S_3-150 sample are uniquely indexed in the orthorhombic Sb_2S_3 (space group: Pbnm). All of these are in accordance with the XRD result. The element distribution of the Sb_2S_3-150 sample was studied using the EDS spectrum in Fig. 3d and demonstrated that the sample is composed of Sb and S elements, while the weight ratio of Sb to S is estimated to be 72.35:27.65. According to the calculation result, the atomic ratio of Sb to S is very close to 2:3, which further confirms that the product is orthorhombic Sb_2S_3 (space group: Pbnm).

Based on the above experimental results, the generation of hollow microsphere structures may be ascribed to the Ostwald ripening process, which has been extensively studied by many researchers in recent years [31, 32]. The possible mechanism involved in the formation of hollow microsphere structures is as follows: Sb_2S_3 nanoparticles are produced at the preliminary stages and interconnected to form nanowires. Then, a mass of nanowires is densely aggregated and coarsen. With increasing reaction temperature, these nanowires are stacked to generate hollow microspheres.
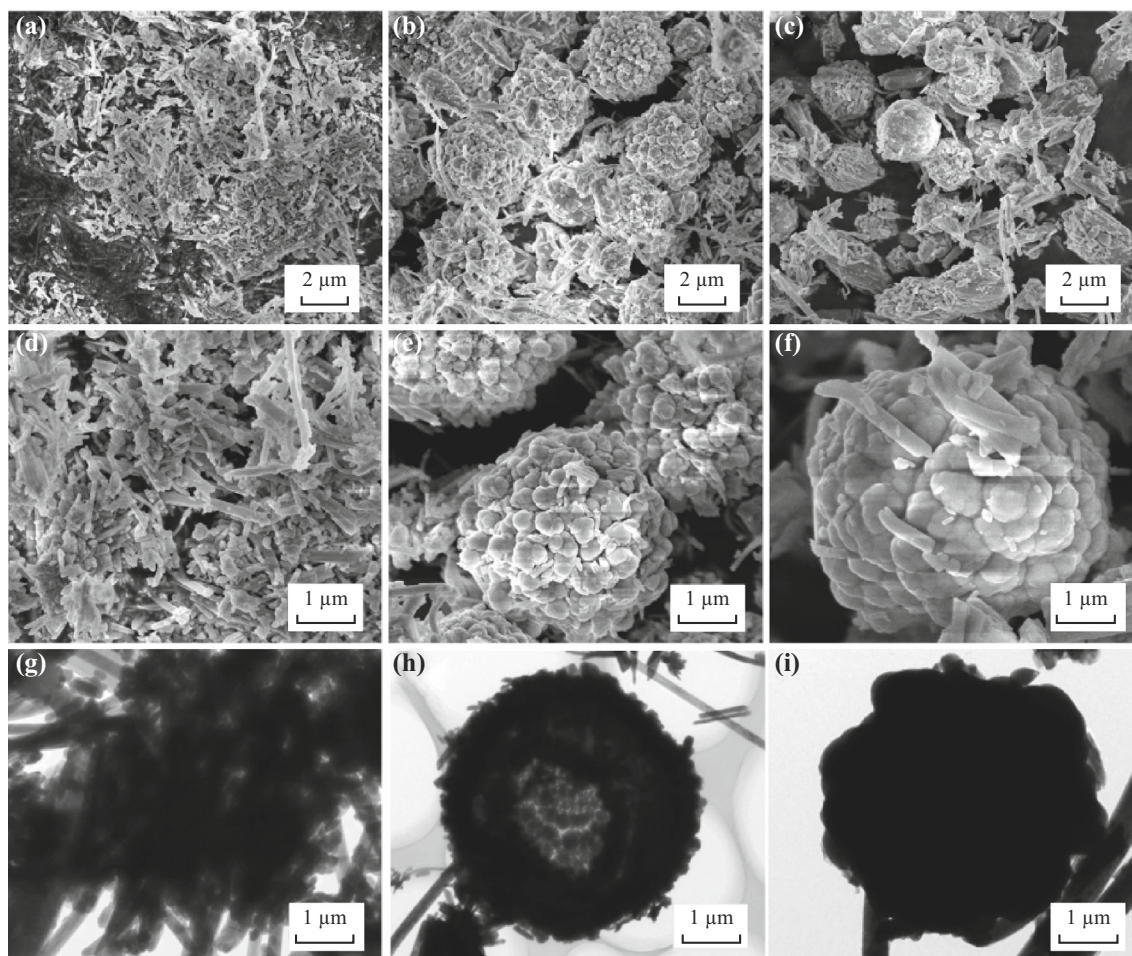
Fig. 2 **a**-**f** FIB-SEM and **g**-**i** TEM images of **a**, **d**, **g** Sb_2S_3-120, **b**, **e**, **h** Sb_2S_3-150, and **c**, **f**, **i** Sb_2S_3-180 samples

3.2 Electrochemical Studies in Lithium-Ion Batteries

The cyclic voltammograms (CV) and galvanostatic charge/discharge measurements were taken to assess the electrochemical capability of Sb_2S_3-120, Sb_2S_3-150, and Sb_2S_3-180 as anode materials for LIBs. Figure 4a displays CV curves of the Sb_2S_3-150 electrode for the first three cycles at a scan rate of 0.1 mV s^{-1} in the voltage range of 0.01–2.0 V (vs. Li/Li$^+$). During the first scan, the cathodic peaks are located at 1.23 and 0.67 V corresponding to the conversion reaction of Li with Sb_2S_3 (Eq. 1) and alloying reaction of Li with Sb (Eq. 2), respectively. The anodic peaks that are centered at 1.1, 1.4, and 1.9 V are related to the de-alloying reaction (reverse reaction of Eq. 2) and the formation of Sb_2S_3 (reverse reaction of Eq. 1) [14, 15]. As with the Sb_2S_3-120 electrode (Fig. S2a) and Sb_2S_3-180 electrode (Fig. S2b), the CV curve of Sb_2S_3-150 for the first cathodic scan is different from those of subsequent scans, indicating the presence of an activation process in the initial discharge process [19, 33–35]. From the second

scanning, the stable reduction peak of the conversion reaction is located at 1.7 V and the alloying reaction is located at 0.8 V. The oxidation peaks are stably located, and all the peaks are overlapped, indicating the good electrochemical stability of Sb_2S_3-150. Figure S2a shows the CV scan curves of the Sb_2S_3-120 electrode. During the first scan, the cathodic peaks are located at 1.1 and 1.4 V, and the anodic peaks are located at 0.67 and 1.2 V. The CV scan curves of the Sb_2S_3-180 electrode are exhibited in Fig. S2b. In the first scan, the conversion reaction has anodic and cathodic peaks that are located at 1.85 and 1.2 V, respectively. The anodic peaks of alloying reaction are located at 1.1 and 1.4 V; the cathodic peak is 0.68 V. Remarkably, a polarization overpotential of 0.2 V for the conversion reaction is observed in Sb_2S_3-150 (0.35 V for Sb_2S_3-180), indicating that the voids inside the hollow structure can lead to smaller overpotential and faster reaction kinetics at the electrode surface [10].
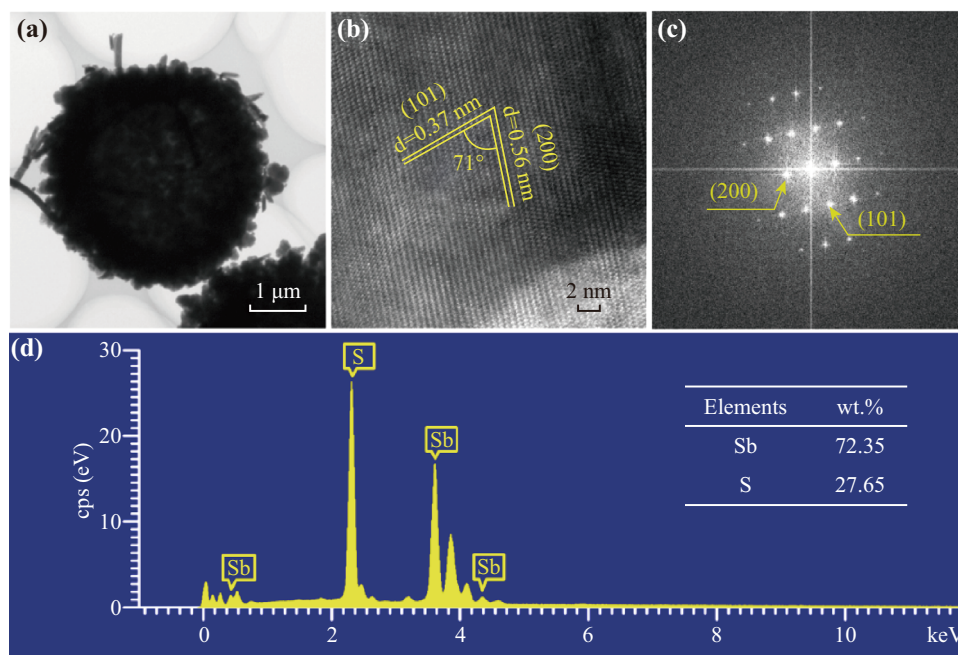
Fig. 3 **a** TEM image of random selected a particle of Sb_2S_3-150 sample. **b** HRTEM image of Sb_2S_3-150 sample taken from **a**. **c** FFT pattern of Sb_2S_3-150 sample. **d** EDS spectrum of Sb_2S_3-150 sample

Conversion reaction: $Sb_2S_3 + 6Li^+ + 6e^- \leftrightharpoons 3Li_2S + 2Sb$ (1)

Alloying reaction: $2Sb + 6Li^+ + 6e^- \leftrightharpoons 2Li_3Sb$ (2)

The rate capability of Sb_2S_3-120, Sb_2S_3-150, and Sb_2S_3-180 electrodes was evaluated at various current densities from 50 to 5000 mA g^{-1} in the voltage range of 0.01–2.0 V (vs. Li/Li$^+$), and the samples were tested for five cycles at each current density. From Fig. 4b, it is observed that Sb_2S_3-150 shows the best rate capability. When cycled at different current densities of 50, 100, 200, 500, 1000, 2000, 3000, 4000, and 5000 mA g^{-1}, the Sb_2S_3-150 electrode presents discharge capacities of 1379, 831, 774, 727, 677, 639, 601, 568, and 541 mAh g^{-1}, respectively. More importantly, the capacity could be quickly recovered after the current density was reduced to 50 mA g^{-1}, indicating excellent rate performance. The Sb_2S_3-120 electrode exhibits a higher discharge capacity than Sb_2S_3-150 at low current densities in the first 20 cycles. Then, it shows a similar specific capacity as Sb_2S_3-150 at current densities of 1000 and 2000 mA g^{-1}. However, as the current densities increase to 3000, 4000, and 5000 mA g^{-1}, Sb_2S_3-150 exhibits a higher specific capacity than Sb_2S_3-120. Sb_2S_3-180 shows a much lower specific capacity than Sb_2S_3-150 at various current densities. The superior rate capability of Sb_2S_3-150 is attributed to its unique hollow microsphere architecture, where the nanosize properties combine with microsize properties to facilitate the rapid transfer of Li$^+$ and electrons [36].

Figure 4c presents the selected charge/discharge voltage profiles of the Sb_2S_3-150 electrode at different current densities in the voltage range of 0.01–2.0 V (vs. Li/Li$^+$). The corresponding profiles of Sb_2S_3-120 and Sb_2S_3-180 are shown in Fig. S3. Compared with Sb_2S_3-120 and Sb_2S_3-180, Sb_2S_3-150 shows a minimal increase in polarization with an increase in current density.

Figure 4d reveals the cycling performance of Sb_2S_3-120, Sb_2S_3-150, and Sb_2S_3-180 at different current densities in the voltage range of 0.01–2.0 V (vs. Li/Li$^+$). It can be seen that their initial discharge/charge capacities of 1369/958, 1281/911, and 1058/767 mAh g^{-1} correspond to initial coulombic efficiencies (CE) of 69%, 71%, and 72.5%, respectively. The major contribution to the additional capacity is attributed to the inevitable formation of solid electrolyte interphase (SEI) film [37, 38]. This phenomenon is normally observed in various metal oxides or sulfide-based anode materials [39–41]. After the first few charge/discharge cycles, the CE rapidly increases to about 99% for all three electrodes. It is determined that the discharge capacity of the Sb_2S_3-150 sample can be kept at about 674 mAh g^{-1} (643 mAh g^{-1} for Sb_2S_3-120 and 532 mAh g^{-1} for Sb_2S_3-180) at a current density of 200 mA g^{-1} after 50 cycles. When the current density increased to 500 mA g^{-1}, there was a slight decrease in the capacity, and it was maintained at about 506 mAh g^{-1} (189 mAh g^{-1} for Sb_2S_3-120 and 234 mAh g^{-1} for Sb_2S_3-180) after 100 cycles. The Sb_2S_3-120 electrode has a higher discharge capacity, but the cycling stability is inferior. The
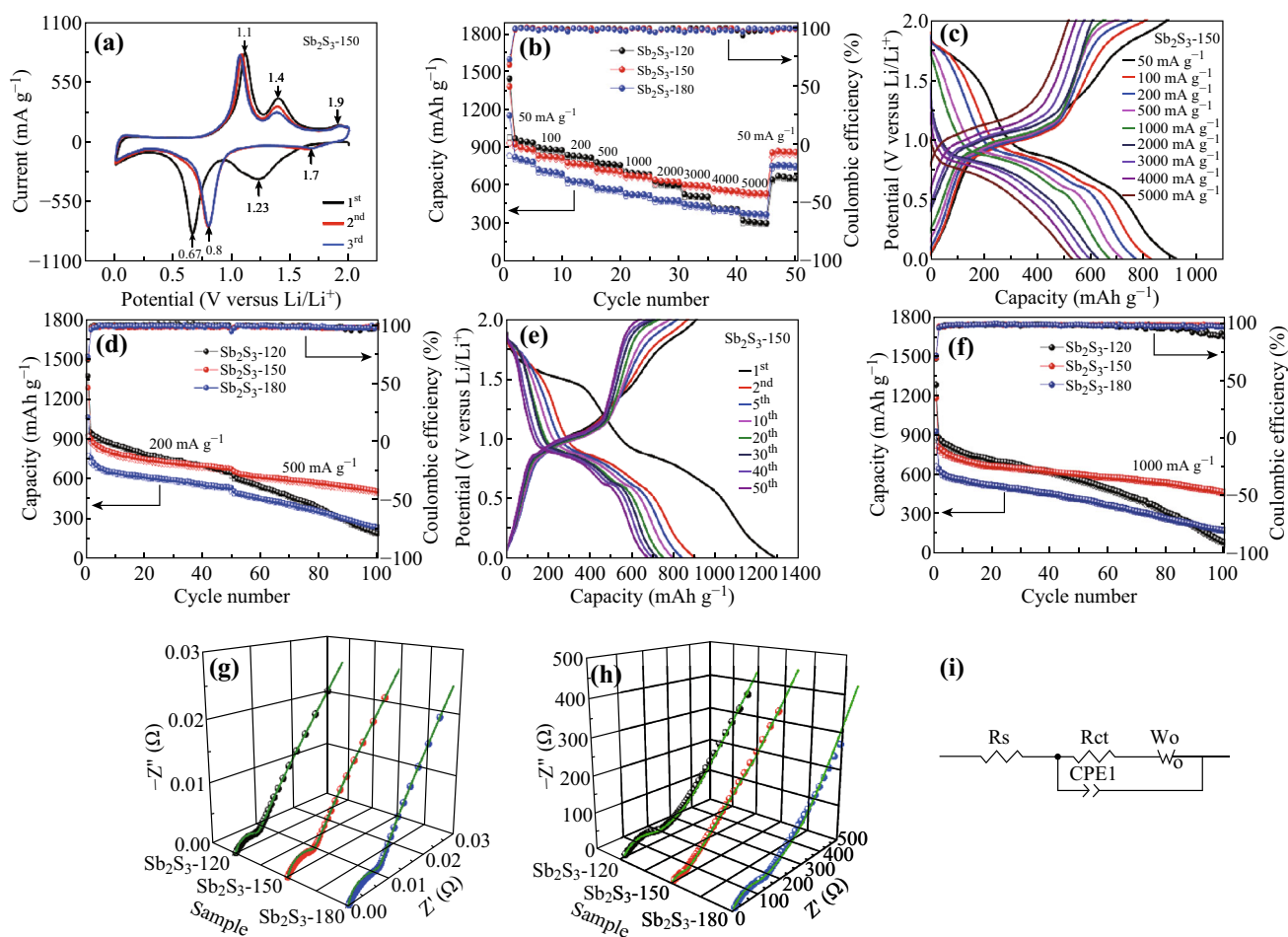
Fig. 4 Excellent lithium-storage performance of as-prepared Sb_2S_3 electrodes. **a** CV curves of Sb_2S_3-150 electrode for the first three cycles at a scan rate of 0.1 mV s^{-1}. **b** Rate performance of Sb_2S_3-120, Sb_2S_3-150, and Sb_2S_3-180 electrodes at various current densities from 50 to 5000 mA g^{-1}. **c** Selected charge/discharge voltage profiles of Sb_2S_3-150 electrode at different current densities (increased from 50 to 5000 mA g^{-1}). **d** Cycling performance of Sb_2S_3-120, Sb_2S_3-150, and Sb_2S_3-180 electrodes at different current densities. **e** Selected charge/discharge voltage profiles of Sb_2S_3-150 electrode at a current density of 200 mA g^{-1}. **f** Cycling performance of Sb_2S_3-120, Sb_2S_3-150, and Sb_2S_3-180 electrodes at a current density of 1000 mA g^{-1}. **g** Three-dimensional Nyquist plots of Sb_2S_3-120, Sb_2S_3-150, and Sb_2S_3-180 electrodes at the open-circuit voltage. **h** Three-dimensional Nyquist plots of Sb_2S_3-120, Sb_2S_3-150 and Sb_2S_3-180 electrodes at a current density of 500 mA g^{-1} after 50 cycles. **i** The equivalent circuit model

Sb_2S_3-150 with a hollow microsphere structure that is used as anode materials for LIBs has a remarkable cycling stability, even though it does not possess any conducting polymer or carbon.

Figure 4e shows the charge/discharge voltage profiles of the Sb_2S_3-150 electrode at a current density of 200 mA g^{-1} in the voltage range of 0.01–2.0 V (vs. Li/Li$^+$). During the initial discharge process, Sb_2S_3 undergoes lithiation via two different mechanisms, which are conversion reaction at $\sim$ 1.4 V and alloying reaction at $\sim$ 0.7 V. During the first charge process, the charge plateau occurs at $\sim$ 1.1, 1.4, and 1.9 V, corresponding to the de-alloying process and the conversion reaction. During the second discharge process, the discharge plateau occurs at $\sim$ 1.7 and 0.8 V. The charge/discharge voltage profile of the Sb_2S_3-150

electrode for the first discharge process is different from that for the second discharge process, indicating the presence of an activation process during the initial discharge process. Furthermore, the voltage plateaus of the charge/discharge profiles of the 50th cycle are perfectly retained. The Sb_2S_3-120 and Sb_2S_3-180 electrodes reveal similar charge/discharge voltage plateaus (Fig. S4), which are in agreement with the CV curves (Fig. S2).

The cycling performance of Sb_2S_3-120, Sb_2S_3-150, and Sb_2S_3-180 electrodes at a high current density of 1000 mA g^{-1} in the voltage range of 0.01–2.0 V (vs. Li/Li$^+$) is verified in Fig. 4f, showing initial coulombic efficiencies of 68%, 69%, and 72%, respectively. It should be noted that the Sb_2S_3-150 electrode maintains a discharge capacity of 469 mAh g^{-1} with a coulombic efficiency of

Table 1 The R_s and R_{ct} values of Sb$_2$S$_3$-120, Sb$_2$S$_3$-150, and Sb$_2$S$_3$-180 electrodes in LIBs

Sample	R_s (Ω)			R_{ct} (Ω)		
	Sb$_2$S$_3$-120	Sb$_2$S$_3$-150	Sb$_2$S$_3$-180	Sb$_2$S$_3$-120	Sb$_2$S$_3$-150	Sb$_2$S$_3$-180
Before cycle	0.001242	0.001629	0.002298	0.005954	0.007886	0.008348
After 50 cycles	16.83	3.135	3.997	110	65	104

Table 2 Comparison of the performance between hierarchical Sb$_2$S$_3$ hollow microspheres with other reported Sb$_2$S$_3$ in studies as anode materials for LIBs

Synthesis method	Samples	Voltage range (V)	Current density (mA g^{-1})	Capacity (mAh g^{-1}) (cycle number)
Hydrothermal reaction [16]	Sb$_2$S$_3$	0.01–3.0	50	914(1)–175(10)
Two-step oxidation-sulfuration route [18]	Sb$_2$S$_3$	0.01–3.0	100	1187.2(1)–548(100)
Hydrothermal reaction [50]	Sb$_2$S$_3$	0–2.5	400	1049(1)–286(20)
Hydrothermal reaction [51]	Sb$_2$S$_3$	0.01–3.0	50	1070(1)–367(25)
Three-step wet-chemical synthesis method [34]	rGO-Sb$_2$S$_3$	0–2.5	250	880(1)–720(50)
Solvothermal treatment [52]	Sb$_2$S$_3$/C	0.01–2.5	100	1084(1)–960(30)
Hydrothermal reaction and mechanical milling [53]	Sb$_2$S$_3$-graphite	0.01–2.8	1000	720(1)–656(100)
Solid-state routes [54]	Sb$_2$S$_3$/C	0–2.5	100	757(1)–600(100)
Present work: hydrothermal reaction	Sb$_2$S$_3$	0.01–2.0	1000	1185(1)–469(100)

98% after 100 cycles (90 mAh g^{-1} for Sb$_2$S$_3$-120 and 179 mAh g^{-1} for Sb$_2$S$_3$-180), manifesting superior cyclability. This is because the interior hollow structure can provide sufficient space to mitigate the volume change and pulverization, which is caused by the Li$^+$ insertion/extraction [42–45]. For Sb$_2$S$_3$-120, the discharge capacity is higher than Sb$_2$S$_3$-150 and Sb$_2$S$_3$-180 in the first 30 cycles, but it decreases gradually and has a residual capacity of 90 mAh g^{-1} with a coulombic efficiency of 88% after 100 cycles. The higher discharge capacity of Sb$_2$S$_3$-120 is due to the nanowire size. During repeated insertion and extraction, the volume change and pulverization are the main causes attributed to the serious attenuation. For Sb$_2$S$_3$-180, the solid spherical structures affect the full contact between the electrolyte and active material, as well as the diffusion of Li$^+$.

To further investigate the dynamics for lithium insertion and extraction of the Sb$_2$S$_3$-150 electrode, EIS measurements of Sb$_2$S$_3$-120, Sb$_2$S$_3$-150, and Sb$_2$S$_3$-180 electrodes were taken. The homologous 3D Nyquist plots are composed of an oblique line in the low-frequency region and a semicircle in the high-frequency region [46, 47]. The EIS data were analyzed by fitting with an equivalent electrical circuit model (Fig. 4i), and the fitted impedance data are listed in Table 1, where the oblique line is related to the Li$^+$ diffusion within the active material, and the semicircle is applicable to the charge-transfer resistance (R_{ct}) between the electrolyte and active material [48, 49]. It is clear that the fitting patterns are consistent with the experimental EIS data. Before cycling, the Sb$_2$S$_3$-120 sample shows a lower
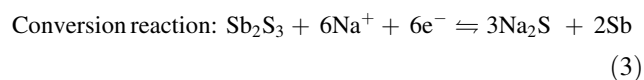
R_{ct} (Fig. 4g) than the Sb$_2$S$_3$-150 and Sb$_2$S$_3$-180 samples because the small size structure can provide additional reaction sites. After 50 cycles at a current density of 500 mA g^{-1} in the voltage range of 0.01–2.0 V (vs. Li/Li$^+$), the R_{ct} of the Sb$_2$S$_3$-120 and Sb$_2$S$_3$-180 electrodes increases to 110 and 104 Ω, respectively (Fig. 4h). However, the R_{ct} of the Sb$_2$S$_3$-150 electrode only increases to 65 Ω, which is much less than that for the Sb$_2$S$_3$-120 and Sb$_2$S$_3$-180 electrodes, indicating that the 3D hollow microsphere structure of the Sb$_2$S$_3$-150 electrode can effectively enhance the diffusion ability of Li$^+$ and facilitate charge transfer.

Table 2 compares the synthesis method and electrochemical properties between hierarchical Sb$_2$S$_3$ hollow microspheres and other reported Sb$_2$S$_3$ in studies as anode materials for LIBs. As seen in the table, the hierarchical Sb$_2$S$_3$ hollow microspheres display superior electrochemical performance among unmodified Sb$_2$S$_3$ samples [16, 18, 50, 51]. Although the Sb$_2$S$_3$ obtained by the two-step oxidation–sulfuration method [18] achieved a higher discharge capacity of 548 mAh g^{-1} after 100 cycles, it should be noted that these data were acquired at a much lower current density of 100 mA g^{-1} and a wider voltage range (0.01–3.0 V). The Sb$_2$S$_3$-carbon composites, such as rGO-Sb$_2$S$_3$ [34] and Sb$_2$S$_3$/C [52], showed much better cycling stability than bare Sb$_2$S$_3$, which delivered the high specific capacity of 720 and 960 mAh g^{-1} after 50 and 30 cycles at a current density of 250 and 100 mA g^{-1}, respectively. Nonetheless, the electrochemical properties at a high current density of 1000 mA g^{-1} were not

mentioned. The Sb_2S_3/C prepared using the solid-state method [53] offered a high specific capacity of 600 mAh g^{-1} after 100 cycles, but this result was also obtained at a lower current density of 100 mA g^{-1}. Sb_2S_3-graphite prepared by hydrothermal reaction and mechanical milling [54] exhibited an outstanding electrochemical performance of 656 mAh g^{-1} at a current density of 1000 mA g^{-1} after 100 cycles. Remarkably, the electrochemical performance of hierarchical Sb_2S_3 hollow microspheres in this work is comparable even with the previously reported Sb_2S_3-carbon composites. Meanwhile, it is widely accepted that composites with graphite or carbon can effectively improve the cyclability. In future work, the electrochemical properties of Sb_2S_3 hollow microspheres will be further improved by the addition of carbon-based materials.

3.3 Electrochemical Studies with Sodium-Ion Batteries

Based on the excellent lithium-storage performance, it is important to attempt to extend the sodium-storage properties of the Sb_2S_3-120, Sb_2S_3-150, and Sb_2S_3-180 samples. The CV curves of hollow microsphere Sb_2S_3-150 electrodes for the initial three cycles at a scan rate of 0.1 mV s^{-1} in the voltage range of 0.01–2.0 V (vs. Na/Na$^+$) are displayed in Fig. 5a. In the first cathodic scanning, the reduction peaks that are centered at 1.1, 0.8, and 0.44 V can be attributed to the conversion reaction between Sb_2S_3 and Na (Eq. 3), as well as the alloying reaction of Sb with Na (Eq. 4). The first anodic scanning gives two oxidation peaks that are stably centered at 0.78 and 1.33 V, resulting from the de-alloying reaction (reverse reaction of Eq. 4) and conversion reaction (reverse reaction of Eq. 3), respectively [15, 55]. During the subsequent scanning, the reduction peaks of the conversion reaction are located at 1.27 V, the alloying reaction are located at 0.4 and 0.85 V, and all of the peaks overlap very well, indicating that the hollow microsphere Sb_2S_3-150 sample has good stability.

$$\text{Conversion reaction: } Sb_2S_3 + 6Na^+ + 6e^- \leftrightharpoons 3Na_2S + 2Sb \tag{3}$$

$$\text{Alloying reaction: } 2Sb + 6Na^+ + 6e^- \leftrightharpoons 2Na_3Sb \tag{4}$$

The rate capabilities of Sb_2S_3-120, Sb_2S_3-150, and Sb_2S_3-180 electrodes were each assessed at current densities of 50, 100, 200, 500, 1000, 2000, 3000, 4000, and 5000 mA g^{-1} for five cycles in the voltage range of 0.01–2.0 V (vs. Na/Na$^+$) (Fig. 5b). As with the lithium-storage performance, the Sb_2S_3-120 electrode also exhibits a higher discharge capacity at low current densities during the first few cycles. Sb_2S_3-180 shows the lowest specific capacity. The Sb_2S_3-150 electrode provides a discharge

capacity of 990 mAh g^{-1} at a current density of 50 mA g^{-1}. When the current density increases to 100, 200, 500, 1000, 2000, 3000, 4000, and 5000 mA g^{-1}, the discharge capacity moderately decreases to 645, 582, 537, 463, 386, 314, 275, and 239 mAh g^{-1}, respectively. When the current density decreases to 50 mA g^{-1}, the reversible capacity can recover to 629 mAh g^{-1}, indicating the distinguished rate capability of the Sb_2S_3-150 electrode, which may originate from the unique hierarchical hollow structure.

Figure 5c exhibits the cycling property of Sb_2S_3-120, Sb_2S_3-150, and Sb_2S_3-180 electrodes at a current density of 200 mA g^{-1}, and the first discharge/charge capacities of 1069/656, 988/616, and 831/551 mAh g^{-1}, with coulombic efficiencies of 61%, 62%, and 66%, respectively. The much lower initial specific capacity relative to that of LIB (1370/958, 1281/912, and 1058/767 mAh g^{-1}) may be related to the slower ionic diffusion rate during the charging/discharging process in NIBs, which is due to the relatively large ionic radius of Na$^+$ (102 pm) compared to that of Li$^+$ (76 pm) [12, 56]. Interestingly, the Sb_2S_3-150 electrode exhibits good cycling stability and still provides a reversible capacity of 384 mAh g^{-1} with a coulombic efficiency of 98% after 50 cycles. For Sb_2S_3-120 and Sb_2S_3-180 electrodes, the capacities are stable for the initial 20 cycles, but decreases gradually, and has residual discharge capacities of 49 and 103 mAh g^{-1} (with coulombic efficiencies of 90% and 94%) after 50 cycles, respectively. These data verify that Sb_2S_3-150 with hollow microsphere structures can be a promising candidate anode material for NIBs.

The charge/discharge voltage profiles of the Sb_2S_3-150 electrode for the initial five cycles at a current density of 200 mA g^{-1} are shown in Fig. 5d. The first discharge voltage profile shows an obvious voltage platform located at $\sim$1.1, 0.8, and 0.4 V, which is related to the conversion reaction and alloying reaction. The first charge–voltage profile exhibits a visible voltage platform located at $\sim$0.8 and 1.3 V, corresponding to the de-alloying reaction and conversion reaction, respectively. In the subsequent cycling, the discharge voltage plateaus of the conversion reaction are located at $\sim$1.2 and 0.8 V and the alloying reaction are located at 0.4 V, which is consistent with the CV results (Fig. 5a).

To further explain the prominent sodium-storage electrochemical behavior of Sb_2S_3-150 electrodes, EIS measurements of Sb_2S_3-120, Sb_2S_3-150, and Sb_2S_3-180 electrodes were taken. The inset of Fig. 5f shows the equivalent circuit model, which is in accordance with LIBs (Fig. 4i), and the fitted impedance data are recorded in Table 3. The R_{ct} value of the hollow microsphere Sb_2S_3-150 electrode is 0.21 Ω (0.11 Ω for Sb_2S_3-120, 0.245 Ω for Sb_2S_3-180) before cycling. Nevertheless, the R_{ct} value of
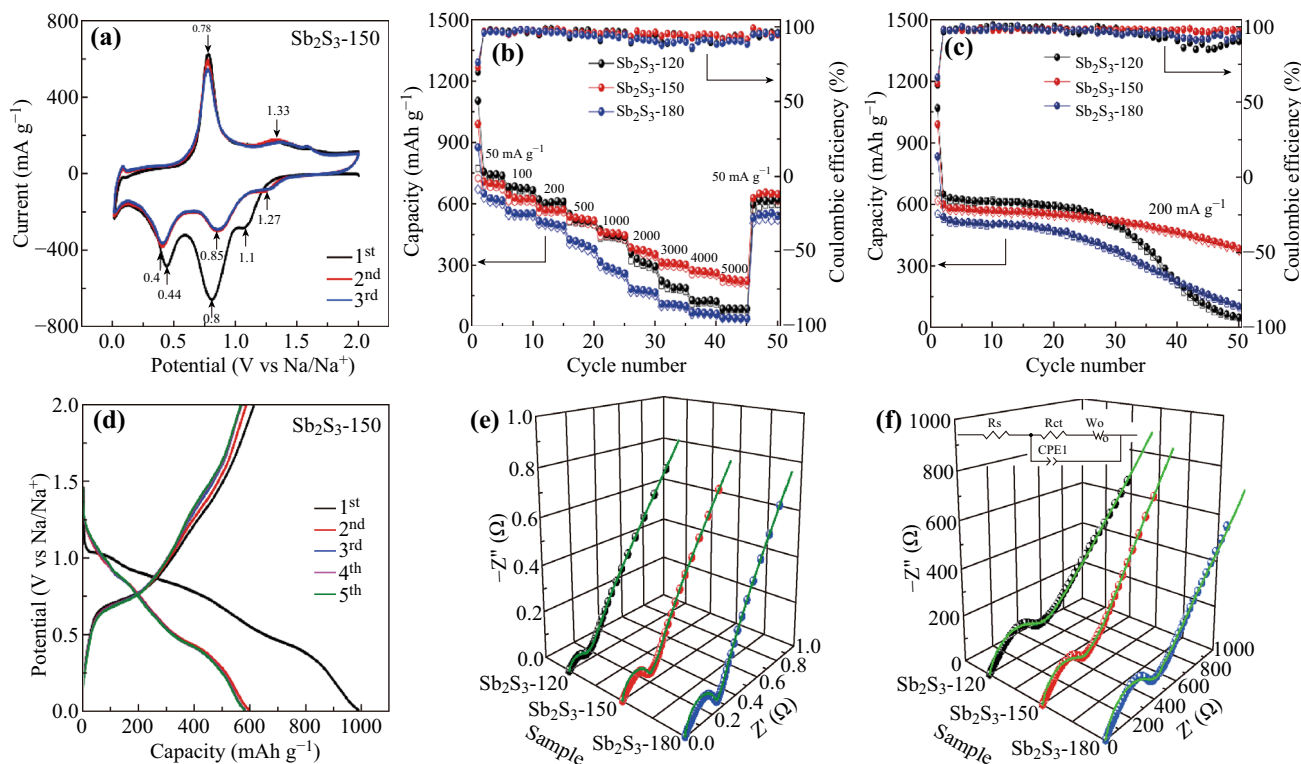
Fig. 5 Excellent sodium-storage performance of as-prepared Sb_2S_3 electrodes. **a** CV curves of Sb_2S_3-150 in first three cycles with a scan rate of 0.1 mV s^{-1}. **b** Rate capability of the Sb_2S_3-120, Sb_2S_3-150 and Sb_2S_3-180 at various current densities (increased from 50 to 5000 mA g^{-1}). **c** Cycle performance of the Sb_2S_3-120, Sb_2S_3-150 and Sb_2S_3-180 electrodes at a current density of 200 mA g^{-1}. **d** Charge/discharge voltage profiles of Sb_2S_3-150 electrode for the first five cycles at a current density of 200 mA g^{-1}. **e** Three-dimensional Nyquist plots of Sb_2S_3-120, Sb_2S_3-150, and Sb_2S_3-180 electrodes at the open-circuit voltage. **f** Three-dimensional Nyquist plots of Sb_2S_3-120, Sb_2S_3-150, and Sb_2S_3-180 electrodes at a current density of 500 mA g^{-1} after 50 cycles (the inset is the equivalent circuit model)

Table 3 The R_s and R_{ct} values of Sb_2S_3-120, Sb_2S_3-150, and Sb_2S_3-180 electrodes in NIBs

Sample	R_s (Ω)			R_{ct} (Ω)		
	Sb_2S_3-120	Sb_2S_3-150	Sb_2S_3-180	Sb_2S_3-120	Sb_2S_3-150	Sb_2S_3-180
Before cycle	0.04429	0.04819	0.05202	0.11	0.21	0.245
After 50 cycles	6.521	5.305	6.455	360	280	350

the Sb_2S_3-150 electrode increases to 280 Ω at a current density of 500 mA g^{-1} after 50 cycles in the voltage range of 0.01–2.0 V (vs. Na/Na$^+$). Meanwhile, the R_{ct} value of Sb_2S_3-120 and Sb_2S_3-180 electrodes increases to 360 and 350 Ω, which is much larger than the hollow microsphere-structured Sb_2S_3-150 electrode. This result infers that Sb_2S_3-150 compared to Sb_2S_3-120 and Sb_2S_3-180 electrodes has a relatively good electrochemical performance.

Table 4 compares the synthesis method and electrochemical properties between hierarchical Sb_2S_3 hollow microspheres and other reported Sb_2S_3 in studies as anode materials for NIBs. As can be seen, the hierarchical Sb_2S_3 hollow microspheres in this work present excellent electrochemical performance compared to the reported Sb_2S_3 microtubes [20]. In addition, it is even comparable with the

reported Sb_2S_3 synthesized reflux process [14] and a-Sb_2S_3 obtained using the polyol-mediated process [57], which was obtained at a lower current density of 50 mA g^{-1}. Nevertheless, compared to that of the previously reported Sb_2S_3-carbon composites, such as Sb_2S_3/C [58], rGO/Sb_2S_3 prepared using the solution-based synthesis technique [19], Sb_2S_3/RGO [47], Sb_2S_3/SGS synthesized using a modified Hummers' method [55], Sb_2S_3 in a P/C composite obtained by a mechanochemical process with heat treatment [59], Sb_2S_3@C [60], MWNTs@Sb_2S_3@PPy prepared using the two-step wet-chemical synthesis method [61], and ZnS-Sb_2S_3@C synthesized by the microthermal solvothermal sulfidation process [62], the electrochemical performance of hierarchical Sb_2S_3 hollow microspheres in this work is lower. It can be deduced that Sb_2S_3 as an anode

Table 4 Comparison of the performance between hierarchical Sb_2S_3 hollow microspheres with other reported Sb_2S_3 in studies as anode materials for LIBs

Synthesis method	Samples	Voltage range (V)	Current density (mA g^{-1})	Capacity (mAh g^{-1}) (cycle number)
One-step hydrothermal method [20]	Sb_2S_3	0–1.5	100	910(1)–201(20)
Reflux process [14]	Sb_2S_3	0.01–2.0	50	970(1)–835.3(50)
Polyol-mediated process [57]	a-Sb_2S_3	0.01–2.5	50	650(1)–512(100)
Hydrothermal reaction [58]	Sb_2S_3/C	0–2.0	100	1200(1)–570(100)
Solution-based synthesis technique [19]	rGO/Sb_2S_3	0–2.0	50	660(1)–670(50)
Hydrothermal reaction [47]	Sb_2S_3/RGO	0.005–3.0	50	1170(1)–581.2(50)
A modified Hummers' method [55]	Sb_2S_3/SGS	0.01–2.5	2000	720(1)–524.4(900)
Mechanochemical process with heat treatment [59]	Sb_2S_3 in P/C	0.005–2.0	50	818(1)–611(100)
Hydrothermal reaction [60]	Sb_2S_3@C	0.01–2.5	100	1066(1)–730(100)
Two-step wet-chemical synthesis method [61]	MWNTs@Sb_2S_3@PPy	0–2	100	870 (1)–500(85)
Microthermal solvothermal sulfidation process [62]	ZnS-Sb_2S_3@C	0.01–1.8	100	1660(1)–630(120)
Present work: hydrothermal reaction	Sb_2S_3	0.01–2.0	200	988(1)–384(50)

material for NIBs possesses more serious capacity fading, and the adding carbon-based materials can enhance the cycling stability of Sb_2S_3 obviously. The capacity fading can be attributed to the relatively large ionic radius of Na$^+$ compared to that of Li$^+$, which gives rise to a series of problems, such as large variations in volume, severe pulverization, and slow ionic diffusion rate during the repeated charging/discharging process in NIBs [6, 10, 63]. These issues cause poor reversibility and low rate capacity. So, it is important to improve the electrochemical properties of Sb_2S_3 hollow microspheres in this work by coating or developing composites using carbon-based materials, making the development of high-performance Sb_2S_3 anode materials for NIBs challenging.

4 Conclusion

In summary, a straightforward and inexpensive hydrothermal method was employed to prepare Sb_2S_3 with a hollow microsphere architecture. Such a unique structure combines the merit of the nanometer size and self-assembly capabilities, achieving a large contact surface area between the electrolyte and active material, short diffusion path for the Li$^+$/Na$^+$ and electron, and additional space to accommodate volume expansion caused by Li$^+$/Na$^+$ insertion/extraction during the repeated charging/discharging process. The resultant Sb_2S_3 hollow microspheres exhibit desirable electrochemical properties, such as high capacity and remarkable reversibility, when used as an anode material in LIBs. A large discharge capacity of 458 mAh g^{-1} at a current density of 1000 mA g^{-1} after 100 cycles is achieved. The Sb_2S_3 hollow microspheres

also reveal remarkable rate capability and cycling performance as anode material for NIBs, keeping a reversible discharge capacity of 384 mAh g^{-1} at a current density of 200 mA g^{-1} after 50 cycles. These prominent lithium/sodium-storage performance enable the hollow microsphere Sb_2S_3 to become competitive among many anode materials reported for LIBs/NIBs. In the future, the cycle performance can be further improved by using graphene compounds (or other conducting polymers).

References

1. M. Obrovac, V. Chevrier, Alloy negative electrodes for Li-ion batteries. Chem. Rev. **114**(23), 11444–11502 (2014). doi:10.1021/cr500207g
2. H. Wang, Y. Wang, Y. Li, Y. Wan, Q. Duan, Exceptional electrochemical performance of nitrogen-doped porous carbon for lithium storage. Carbon **82**, 116–123 (2015). doi:10.1016/j.carbon.2014.10.041

3. K. Xu, Electrolytes and interphases in Li-ion batteries and beyond. Chem. Rev. **114**(23), 11503–11618 (2014). doi:10.1021/cr500003w

4. J.B. Goodenough, K.-S. Park, J. Am, The Li-ion rechargeable battery: a perspective. J. Am. Chem. Soc. **135**(4), 1167–1176 (2013). doi:10.1016/j.bcdf.2016.09.001

5. H. Wang, Y. Zhou, Y. Shen, Y. Li, Q. Zuo, Q. Duan, Fabrication, formation mechanism and the application in lithium-ion battery of porous Fe_2O_3 nanotubes via single-spinneret electrospinning. Electrochim. Acta **158**(21), 105–112 (2015). doi:10.1016/j.electacta.2015.01.149

6. D. Kundu, E. Talaie, V. Duffort, L.F. Nazar, The emerging chemistry of sodium ion batteries for electrochemical energy storage. Angew. Chem. Int. Ed. **54**(11), 3431–3448 (2015). doi:10.1002/anie.201410376

7. Y. Kim, K.H. Ha, S.M. Oh, K.T. Lee, High-capacity anode materials for sodium-ion batteries. Chem. Eur. J. **20**(38), 11980–11992 (2014). doi:10.1002/chem.201402511

8. N. Yabuuchi, K. Kubota, M. Dahbi, S. Komaba, Research development on sodium-ion batteries. Chem. Rev. **114**(23), 11636–11682 (2014). doi:10.1021/cr500192f

9. L. Wang, Y. Lu, J. Liu, M. Xu, J. Cheng, D. Zhang, J.B. Goodenough, A superior low-cost cathode for a Na-ion battery. Angew. Chem. Int. Ed. **52**(7), 1964–1967 (2013). doi:10.1002/anie.201206854

10. Y. Zhao, A. Manthiram, $Bi_{0.94}Sb_{1.06}S_3$ nanorod cluster anodes for sodium-ion batteries: enhanced reversibility by the synergistic effect of the Bi_2S_3-Sb_2S_3 solid solution. Chem. Mater. **27**(17), 6139–6145 (2015). doi:10.1021/acs.chemmater.5b02833

11. Y. Jiang, M. Wei, J. Feng, Y. Ma, S. Xiong, Enhancing the cycling stability of Na-ion batteries by bonding SnS_2 ultrafine nanocrystals on amino-functionalized graphene hybrid nanosheets. Energy Environ. Sci. **9**(4), 1430–1438 (2016). doi:10.1039/c5ee03262h

12. Z. Yi, Q. Han, X. Li, Y. Wu, Y. Cheng, L. Wang, Two-step oxidation of bulk Sb to one-dimensional Sb_2O_4 submicron-tubes as advanced anode materials for lithium-ion and sodium-ion batteries. Chem. Eng. J. **315**, 101–107 (2017). doi:10.1016/j.cej.2017.01.020

13. A.L. Hameed, M. Reddy, J. Cheng, B. Chowdari, J.J. Vittal, RGO/stibnite nanocomposite as a dual anode for lithium and sodium ion batteries. ACS Sustainable Chem. Eng. **4**(5), 2479–2486 (2016). doi:10.1021/acssuschemeng.5b01211

14. Y. Zhu, P. Nie, L. Shen, S. Dong, Q. Sheng, H. Li, H. Luo, X. Zhang, High rate capability and superior cycle stability of a flower-like Sb_2S_3 anode for high-capacity sodium ion batteries. Nanoscale **7**(7), 3309–3315 (2015). doi:10.1039/C4NR05242K

15. Y. Liu, L.-Z. Fan, L. Jiao, Graphene highly scattered in porous carbon nanofibers: a binder-free and high-performance anode for sodium-ion batteries. J. Mater. Chem. A **5**(4), 1698–1705 (2017). doi:10.1039/C6TA09961K

16. C. Yan, G. Chen, D. Chen, J. Pei, J. Sun, H. Xu, Y. Zhang, Z. Qiu, Double surfactant-directed controllable synthesis of Sb_2S_3 crystals with comparable electrochemical performances. CrystEngComm **16**(33), 7753–7760 (2014). doi:10.1039/c4ce00871e

17. X. Zhou, S. Hua, L. Bai, D. Yu, Synthesis and electrochemical performance of hierarchical Sb_2S_3 nanorod-bundles for lithium-ion batteries. J. Electrochem. Sci. Eng. **4**(2), 45–53 (2014). doi:10.5599/jese.2014.0045

18. Z. Yi, Q.G. Han, Y. Cheng, Y.M. Wu, L.M. Wang, Facile synthesis of symmetric bundle-like Sb_2S_3 micron-structures and their application in lithium-ion battery anodes. Chem. Commun. **52**(49), 7691–7694 (2016). doi:10.1039/c6cc03176e

19. Y. Denis, P.V. Prikhodchenko, C.W. Mason, S.K. Batabyal, J. Gun, S. Sladkevich, A.G. Medvedev, O. Lev, High-capacity antimony sulphide nanoparticle-decorated graphene composite as anode for sodium-ion batteries. Nat. Commun. **4**(4), 2922 (2013). doi:10.1038/ncomms3922

20. J. Pan, Z.-L. Zuo, J.-Q. Deng, J. Wang, C.-C. Fang, Q.-R. Yao, Template-free synthesis of Sb_2S_3 micro tubes as the anode materials for sodium-ion batteries. Int Conf Adv Mater Energy Sust (2017). doi:10.1142/9789813220393_0010

21. Z. Zhang, L. Li, Q. Xu, B. Cao, 3D hierarchical Co_3O_4 microspheres with enhanced lithium-ion battery performance. RSC Adv. **5**(76), 61631–61638 (2015). doi:10.1039/c5ra11472a

22. L. Shen, L. Yu, X.Y. Yu, X. Zhang, X.W.D. Lou, Self-templated formation of uniform $NiCo_2O_4$ hollow spheres with complex interior structures for lithium-ion batteries and supercapacitors. Angew. Chem. Int. Ed. **54**(6), 1868–1872 (2015). doi:10.1002/ange.201409776

23. H. Sun, G. Xin, T. Hu, M. Yu, D. Shao, X. Sun, J. Lian, High-rate lithiation-induced reactivation of mesoporous hollow spheres for long-lived lithium-ion batteries. Nat. Commun. **5**(7), 4526 (2014). doi:10.1038/ncomms5526

24. J. Wang, N. Yang, H. Tang, Z. Dong, Q. Jin, M. Yang, D. Kisailus, H. Zhao, Z. Tang, D. Wang, Accurate control of multishelled Co_3O_4 hollow microspheres as high-performance anode materials in lithium-ion batteries. Angew. Chem. Int. Ed. **125**(25), 6545–6548 (2013). doi:10.1002/ange.201301622

25. S. Xu, C.M. Hessel, H. Ren, R. Yu, Q. Jin, M. Yang, H. Zhao, D. Wang, α-Fe_2O_3 multi-shelled hollow microspheres for lithium ion battery anodes with superior capacity and charge retention. Energy Environ. Sci. **7**(2), 632–637 (2014). doi:10.1039/c3ee43319f

26. X.M. Yin, C.C. Li, M. Zhang, Q.Y. Hao, S. Liu, L.B. Chen, T.H. Wang, One-step synthesis of hierarchical SnO_2 hollow nanostructures via self-assembly for high power lithium ion batteries. J. Phys. Chem. C **114**(17), 8084–8088 (2010). doi:10.1021/jp100224x

27. D. Ma, Z. Cao, A. Hu, Si-Based anode materials for Li-ion batteries: a mini review. Nano-Micro Lett. **6**(4), 347–358 (2014). doi:10.1007/s40820-014-0008-2

28. G. Zhang, X.W.D. Lou, General synthesis of multi-shelled mixed metal oxide hollow spheres with superior lithium storage properties. Angew. Chem. Int. Ed. **126**(34), 9187–9190 (2014). doi:10.1002/ange.201404604

29. Q. Wang, L. Zhu, L. Sun, Y. Liu, L. Jiao, Facile synthesis of hierarchical porous $ZnCo_2O_4$ microspheres for high-performance supercapacitors. J. Mater. Chem. **3**(3), 982–985 (2015). doi:10.1039/c4ta05279j

30. L. Cao, D. Chen, R.A. Caruso, Surface-metastable phase-initiated seeding and Ostwald ripening: a facile fluorine-free process towards spherical fluffy core/shell, yolk/shell, and hollow anatase nanostructures. Angew. Chem. Int. Ed. **52**(42), 10986–10991 (2013). doi:10.1002/ange.201305819

31. A. Pan, H. Wu, L. Yu, X. Lou, Template-free synthesis of VO_2 hollow microspheres with various interiors and their conversion into V_2O_5 for lithium-ion batteries. Angew. Chem. Int. Ed. **125**(8), 2282–2286 (2013). doi:10.1002/ange.201209535

32. H. Xia, J. Zhang, Z. Yang, S.Y. Guo, S.H. Guo, Q. Xu, 2D MOF Nanoflake-assembled spherical microstructures for enhanced supercapacitor and electrocatalysis performances. Nano-Micro Lett. **9**, 43 (2017). doi:10.1007/s40820-017-0144-6

33. S. Wang, S. Yuan, Y.B. Yin, Y.H. Zhu, X.B. Zhang, J.M. Yan, Green and facile fabrication of $MWNTs@Sb_2S_3@PPy$ coaxial nanocables for high-performance Na-ion batteries. Part. Part. Syst. Charact. **33**(8), 493–499 (2016). doi:10.1002/ppsc.201500227

34. P.V. Prikhodchenko, J. Gun, S. Sladkevich, A.A. Mikhaylov, O. Lev, Y.Y. Tay, S.K. Batabyal, D.Y. Yu, Conversion of hydroperoxoantimonate coated graphenes to $Sb_2S_3@graphene$ for

a superior lithium battery anode. Chem. Mater. **24**(24), 4750–4757 (2012). doi:10.1021/cm3031818

35. J. Pan, N. Wang, Y. Zhou, X. Yang, W. Zhou, Y. Qian, J. Yang, Simple synthesis of a porous Sb/Sb$_2$O$_3$ nanocomposite for a high-capacity anode material in Na-ion batteries. Nano Res. **10**(5), 1794–1803 (2017). doi:10.1007/s12274-017-1501-y

36. C. Niu, J. Meng, C. Han, K. Zhao, M. Yan, L. Mai, VO$_2$ nanowires assembled into hollow microspheres for high-rate and long-life lithium batteries. Nano Lett. **14**(5), 2873–2878 (2014). doi:10.1021/nl500915b

37. Y. Hu, Z. Liu, K.-W. Nam, O.J. Borkiewicz, J. Cheng et al., Origin of additional capacities in metal oxide lithium-ion battery electrodes. Nat. Mater. **12**(12), 1130–1136 (2013). doi:10.1038/NMAT3784

38. Y. Dong, M. Yu, Z. Wang, Y. Liu, X. Wang, Z. Zhao, J. Qiu, A top-down strategy toward 3D carbon nanosheet frameworks decorated with hollow nanostructures for superior lithium storage. Adv. Funct. Mater. **26**(42), 7590–7598 (2016). doi:10.1002/adfm.201603659

39. Y.-Y. Hu, Z. Liu, K.-W. Nam, O.J. Borkiewicz, J. Cheng et al., Origin of additional capacities in metal oxide lithium-ion battery electrodes. Nat. Mater. **12**(12), 1130–1136 (2013). doi:10.1038/NMAT3784

40. C. Jiang, C. Yuan, P. Li, H.-G. Wang, Y. Li, Q. Duan, Nitrogen-doped porous graphene with MnO$_2$ nanowires as high-performance anode materials for lithium-ion batteries. J. Mater. Chem. A **4**(19), 7251–7256 (2016). doi:10.1039/C5TA10711C

41. Y. Xu, J. Guo, C. Wang, Sponge-like porous carbon/tin composite anode materials for lithium ion batteries. J. Mater. Chem. **22**(19), 9562–9567 (2012). doi:10.1039/c2jm30448a

42. B. Wang, H.B. Wu, L. Zhang, X.W.D. Lou, Self-supported construction of uniform Fe$_3$O$_4$ hollow microspheres from nanoplate building blocks. Angew. Chem. Int. Ed. **52**(15), 4165–4168 (2013). doi:10.1002/ange.201300190

43. K. Zhu, H. Gao, G. Hu, M. Liu, H. Wang, Scalable synthesis of hierarchical hollow Li$_4$Ti$_5$O$_{12}$ microspheres assembled by zig-zag-like nanosheets for high rate lithium-ion batteries. J. Power Sources **340**, 263–272 (2017). doi:10.1016/j.jpowsour.2016.11.074

44. X. Zhang, J.-G. Wang, H. Liu, H. Liu, B. Wei, Facile synthesis of V$_2$O$_5$ hollow spheres as advanced cathodes for high-performance lithium-ion batteries. Materials **10**(1), 77 (2017). doi:10.3390/ma10010077

45. R. Liu, W. Su, C. Shen, J. Iocozzia, S. Zhao, K. Yuan, N. Zhang, C.-A. Wang, Z. Lin, Hydrothermal synthesis of hollow SnO$_2$ spheres with excellent electrochemical performance for anodes in lithium ion batteries. Mater. Res. Bull. (2017). doi:10.1016/j.materresbull.2017.03.004. **(In press)**

46. D. Wang, Y. Yu, H. He, J. Wang, W. Zhou, H.D. Abruna, Template-free synthesis of hollow-structured Co$_3$O$_4$ nanoparticles as high-performance anodes for lithium-ion batteries. ACS Nano **9**(2), 1775–1781 (2015). doi:10.1021/nn506624g

47. F. Wu, X. Guo, M. Li, H. Xu, One-step hydrothermal synthesis of Sb$_2$S$_3$/reduced graphene oxide nanocomposites for high-performance sodium ion batteries anode materials. Ceram. Int. **43**(8), 6019–6023 (2017). doi:10.1016/j.ceramint.2017.01.141

48. Z. Yan, L. Liu, J. Tan, Q. Zhou, Z. Huang, D. Xia, H. Shu, X. Yang, X. Wang, One-pot synthesis of bicrystalline titanium dioxide spheres with a core-shell structure as anode materials for lithium and sodium ion batteries. J. Power Sources **269**, 37–45 (2014). doi:10.1016/j.jpowsour.2014.06.150

49. J. Tan, L. Liu, S. Guo, H. Hu, Z. Yan et al., The electrochemical performance and mechanism of cobalt (II) fluoride as anode material for lithium and sodium ion batteries. Electrochim. Acta **168**, 225–233 (2015). doi:10.1016/j.electacta.2015.04.029

50. K. Xiao, Q. Xu, K. Ye, Z. Liu, L. Fu, N. Li, Y. Chen, Y. Su, Facile hydrothermal synthesis of Sb$_2$S$_3$ nanorods and their magnetic and electrochemical properties. ECS Solid State Lett. **2**(6), 51–54 (2013). doi:10.1149/2.007306ssl

51. J. Ma, X. Duan, J. Lian, T. Kim, P. Peng, X. Liu, Z. Liu, H. Li, W. Zheng, Sb$_2$S$_3$ with various nanostructures: controllable synthesis, formation mechanism, and electrochemical performance toward lithium storage. Chem. Eur. J. **16**(44), 13210–13217 (2010). doi:10.1002/chem.201000962

52. X. Zhou, L. Bai, J. Yan, S. He, Z. Lei, Solvothermal synthesis of Sb$_2$S$_3$/C composite nanorods with excellent Li-storage performance. Electrochim. Acta **108**(10), 17–21 (2013). doi:10.1016/j.electacta.2013.06.049

53. C.-M. Park, Y. Hwa, N.-E. Sung, H.-J. Sohn, Stibnite (Sb$_2$S$_3$) and its amorphous composite as dual electrodes for rechargeable lithium batteries. J. Mater. Chem. **20**(6), 1097–1102 (2010). doi:10.1039/b918220a

54. Y. Zhao, A. Manthiram, Amorphous Sb$_2$S$_3$ embedded in graphite: a high-rate, long-life anode material for sodium-ion batteries. Chem. Commun. **51**(67), 13205–13208 (2015). doi:10.1039/C5CC03825A

55. X. Xiong, G. Wang, Y. Lin, Y. Wang, X. Ou, F. Zheng, C. Yang, J.-H. Wang, M. Liu, Enhancing sodium ion battery performance by strongly binding nanostructured Sb$_2$S$_3$ on sulfur-doped graphene sheets. ACS Nano **10**(12), 10953–10959 (2016). doi:10.1021/acsnano.6b05653

56. J. Liu, L. Yu, C. Wu, Y. Wen, K. Yin et al., New nanoconfined galvanic replacement synthesis of hollow Sb@C yolk-shell spheres constituting a stable anode for high-rate Li/Na-ion batteries. Nano Lett. **17**(3), 2034–2042 (2017). doi:10.1021/acs.nanolett.7b00083

57. S. Hwang, J. Kim, Y. Kim, Y. Kim, Na-ion storage performance of amorphous Sb$_2$S$_3$ nanoparticles: anode for Na-ion batteries and seawater flow batteries. J. Mater. Chem. A **4**(46), 17946–17951 (2016). doi:10.1039/C6TA07838A

58. S. Yao, J. Cui, Z. Lu, Z.-L. Xu, L. Qin, J. Huang, Z. Sadighi, F. Ciucci, J.-K. Kim, Unveiling the Unique phase transformation behavior and sodiation kinetics of 1D van der waals Sb$_2$S$_3$ anodes for sodium ion batteries. Adv. Energy Mater. **7**(8), 1602149 (2017). doi:10.1002/aenm.201602149

59. J.H. Choi, C.-W. Ha, H.-Y. Choi, H.-C. Shin, C.-M. Park, Y.-N. Jo, S.-M. Lee, Sb$_2$S$_3$ embedded in amorphous P/C composite matrix as high-performance anode material for sodium ion batteries. Electrochim. Acta **210**, 588–595 (2016). doi:10.1016/j.electacta.2016.05.190

60. H. Hou, M. Jing, Z. Huang, Y. Yang, Y. Zhang, J. Chen, Z. Wu, X. Ji, One-dimensional rod-like Sb$_2$S$_3$-based anode for high-performance sodium-ion batteries. ACS Appl. Mater. Interfaces **7**(34), 19362–19369 (2015). doi:10.1021/acsami.5b05509

61. S. Wang, S. Yuan, Y. Yin, Y. Zhu, X. Zhang, J. Yan, Green and facile fabrication of MWNTs@ Sb$_2$S$_3$@PPy coaxial nanocables for high-performance Na-ion batteries. Part. Part. Syst. Charact. **33**(8), 493–499 (2016). doi:10.1002/ppsc.201500227

62. S. Dong, C. Li, X. Ge, Z. Li, X. Miao, L. Yin, ZnS-Sb$_2$S$_3$@C core-double shell polyhedron structure derived from metal-organic framework as anodes for high performance sodium ion batteries. ACS Nano **11**(6), 6474–6482 (2017). doi:10.1021/acsnano.7b03321

63. Y. Zhao, A. Manthiram, High-capacity, high-rate Bi-Sb alloy anodes for lithium-ion and sodium-ion batteries. Chem. Mater. **27**(8), 3096–3101 (2015). doi:10.1021/acs.chemmater.5b00616